ABLATION BEHAVIOUR OF C$_F$/UHTC COMPOSITES AT OBLIQUE ANGLES OF ATTACK

Baker B.,[1] Venkatachalam V.,[1] Zoli L.,[2] Vinci A.,[2] Galizia P.,[2] Sciti D.,[2] Binner J.[1]

[1] School of Metallurgy and Materials, University of Birmingham, Edgbaston, Birmingham, UK

[2] ISTEC, Via Granarolo, 64 - 48018 Faenza, Italy

Abstract

Oxy-acetylene torch testing was performed at a range of angles of attack on C$_f$/ZrB$_2$-SiC-Y$_2$O$_3$ composites, from 10° to 90°. The ablation behaviour was studied in-situ with thermography, and the post-ablation morphologies investigated optically and with elemental analysis. Significantly lower surface temperatures were observed at oblique angles of attack leading to less damage in terms of both oxidation extent and material removal. Rudimentary modelling of a gas stream impinging on a perfect surface showed that the angular variation also led to a significant drop in pressure at more oblique angles of attack, with a commensurate increase in shear stress. The surface oxide formed during testing seemed mainly to correspond to the temperature distribution and was apparently more susceptible to damage from higher impinging pressure than shear stress. This study elucidated some interesting aspects of a modified ablation test and showed some new parameter ranges which may be useful in targeted material screening.

1 Introduction

Ultra-high temperature ceramic matrix composites, UHTCMCs, are promising candidate materials for use in rocket engines and for sharp leading edges of hypersonic control surfaces. They are exposed to significant thermomechanical loads and corrosive atmospheres during use [1,2]. Optimising the materials to produce components that are dimensionally stable during the oxidation inherent to the application conditions, and that are resistive to ablation and spalling, is a key development area to move towards commercialisation [3]. UHTCs, whilst possessing high strength and thermal conductivity [4–6], oxidise at reasonably low temperatures in high pO$_2$ environments [7]. In the case of ZrC and HfC, two commonly investigated UHTCs, this is accompanied by an evolution of CO$_x$ gases [8]. The expansion of these gases upon generation can result in open channels leading to enhanced oxygen ingress to the body of the component [8]. The formation of the (Zr/Hf)O$_2$ product can also produce a non-protective porous solid scale, with linear oxidation kinetics seen at temperatures below the melting point of the oxide products [7]. Above this temperature, the fluid melt can act as an oxygen-passivating barrier layer. However, in a scouring gas environment, the mechanical stability of this fluid may be limited and its removal can result in further oxidation of the component leading to catastrophic failure [9]. For the boride UHTCs, ZrB$_2$ and HfB$_2$, oxidation

proceeds via a liquid B_2O_3 intermediate at temperatures below 1000°C [10], which likewise acts as a passivating fluid scale [11]. When integrated to the solid $(Zr/Hf)O_2$ network this adds a certain resistance to aerodynamic denudation. However, at temperatures beyond the vaporisation temperature of B_2O_3, this mechanism of protection is lost and the components are again vulnerable to rampant oxidation.

A proposed method of enhancing the temperature range of these components is in the doping of materials to improve the thermodynamic and mechanical longevity of the passivating liquid-solid hybrid oxide scale [12–14]. There are various explanations of this effect, which involve enhancement of fluid viscosity, wettability and reduction in the vapour pressure. Authors have found success in improving the ablation resistance by addition of SiC in the temperature range <1650°C [15,16], or further modifications involving combinations of other oxides (e.g. Ta) up to a reported 2900°C [17].

Oxyacetylene-torch ('OAT') testing is a cheap and rapid screening method for UHTCMC samples [18–20]. It provides incredibly high heat fluxes of up to around 20 MW m^{-2} in oxidising environments [21] and is significantly easier, faster and cheaper to perform than stagnation pressure tests, arc-jet tests or plasma tunnel tests, though the latter do provide a more holistic representation of the chemothermomechanical environment of interest [22]. However, an area where OAT testing significantly misrepresents the application conditions is the gas speed (and therefore stagnation pressure) incident on the sample, which has been estimated to be around Mach 0.6 [21]. Whilst the samples are heated to the desired temperature and the formation of the expected oxidation products occurs, the coupling of these aspects with a far lower flow speed ensure that the success or failure of the composition being screened is only truly representative of the reduced flow environment. A potential issue is that the relatively mild mechanical regime (when compared to more energy-intensive test methods or the application conditions) permits protection mechanisms to occur that would not be effective in more aggressive conditions, such as the re-entry environment for example. Whilst the OAT test is only ever intended to provide a rough guide to materials selection, its lack of high-speed gas flow can mean that some materials that progress to subsequent stages of testing are found to be unsuitable.

This paper seeks to investigate a simple modification of the OAT method to help probe different aerothermal regimes. It is possible that by modifying the angle of attack (whilst retaining the same heat flux), the force will become distributed between both compressive and shearing modes at the sample surface [23]. Increased shearing modes will affect, and possibly displace, the materials most weakly bonded to the surface. These will inevitably be the adherent oxide scales responsible for oxidation protection. Hence, by manipulating the gas flow, removal of potentially protective material may result in material failure. It is hoped that by probing these effects, artefacts of the test method and ramifications concerning perceived material performance may become easier to identify, in what is nominally the same test environment, as the angle is usually a factor ignored in the literature.

2 Materials and Methods

2.1 Sample production

The samples studied in this work were provided by ISTEC-CNR and were obtained by slurry infiltration and sintering. Unlike conventional bulk ceramics for which a wide array of known processing techniques is available, the processing of UHTCMCs is complicated by the presence of the fibre reinforcement. Powder mixtures are prepared by wet ball milling of the starting powders with SiC grinding media in absolute ethanol (water content <0.05%) for 24 h at 60 rpm. Commercially available powders were used for the preparation of the ceramic

composite materials: ZrB_2 (H.C. Starck, grade B, Germany) and α-SiC (H.C. Starck, Grade UF-25, Germany), carbon fibres (Pitch fibres XN80, NGF, Japan). After ball milling, the powders were completely dried with a rotary evaporator at 90°C and then sieved. With these powders, aqueous suspensions were prepared following the procedures described in ???, the fibre preforms were infiltrated by slurry infiltration and the layers stacked in a 0/90° configuration. The green pellet was cut in a graphite die and consolidated via hot pressing, initially under vacuum at 1900°C and then under a uni-axial pressure of 40 MPa for 15 min.

2.2 Oxyacetylene torch testing

Oxyacetylene torch testing was performed with a bespoke facility at the University of Birmingham. Flow rates of 0.8 m^3 $hour^{-1}$ for acetylene and 1.1 m^3 $hour^{-1}$ were used, obtaining a heat flux of 17 MW m^{-2} for testing at 10 mm distance, with gas speeds of around Mach 0.6. The samples were fixed in a water-cooled graphite sample holder and rotated directly into the flame to begin the test. A video of a typical test can be seen at www.xyz. The front face temperature was measured by both a 2-colour pyrometer (Metis M3, SensorTherm GmbH, Sulzbach, Germany) and an infrared camera (A655sc, FLIR, Wilsonville OR, USA). The rear face temperature was measured with a k-type thermocouple. An image of the facility permitting angled testing is included in Figure 1.

The thermal gradient was investigated using the IR thermal imaging data with ResearchIR (FLIR Systems). This was calibrated with regards to emissivity using the 2-colour pyrometer data. The thermal gradient was compared to the surface damage and phase change distribution, in addition to the hydrodynamic regime inferred from simulations, to confirm the effect of the changing test environment on the sample behaviour. The pyrometer's optical filter allowed viewing of the evolution of the surface morphology.

2.3 Surface and microstructural analysis

Samples were characterised by mass change rate over the regions of interest. The surface phase microstructure was mapped using scanning electron microscopy (SEM, Jeol 7000, Tokyo, Japan) and electron dispersive spectroscopy (EDS, Oxford Instruments, Oxford, UK). Surface profilimetry was performed to correlate against the thermal gradient (InfiniteFocus, Alicona Imaging GmbH, Graz, Austria). Image analysis was performed (ImageJ, National Institute of Health, MA, USA) to calculate the surface oxidation area after appropriate scaling and to compare to the thermograms measured during the test. Images were 'colour thresholded' such that the oxidised areas were included in pixel counting. This was performed manually, with the colour channels selected for each image.

Mass change rate (Δm/Δt) was determined by:

$$\frac{\Delta m}{\Delta t} = \frac{m_{final} - m_{initial}}{\Delta t}$$

120 seconds was the test duration in all cases in this work. A positive Δm/Δt indicates a net mass gain over the duration of the test, due to the formation of oxidation products with a higher mass than the initial sample. A negative value means a net mass loss over the test, indicating loss of material due to ablation or gaseous evolution.

Specific Δm/Δt is the mass change rate calculated divided by the area of the oxidised region.

The oxide scales' crystal structure and phases were examined using X-ray diffraction (XRD, Bruker D8, Coventry UK) and Raman spectroscopy (inVia Reflex, Reinshaw, New Mills, U.K).

2.4 Numerical simulations

The working fluid properties used were that of air at room temperature. The surface pressure and wall shear were analysed across the sample surface.

Numerical simulations were performed in ANSYS Fluent (ANSYS, PA, USA). A schematic diagram in 2 dimensions of the geometry for the 50° angle of attack is shown in Figure 2. A 3D view of the simulation space is shown in Figure 3. An unstructured grid consisting of tetrahedral elements was used. The mesh generation algorithm was retained for all tests and a standard simulation divided the solution area into between 800,000 and 1,000,000 elements.

A finite volume method was used for the solution of the Navier-Stokes equations. A coupled scheme was used for the pressure and velocity, and the PRESTO! scheme was used for pressure discretisation. A second order upwind scheme was used for the momentum calculation, whereas a first order upwind scheme was used for the formulation of the k-ε turbulence equations (standard). Turbulence was expected for the Reynolds number of this flow (~30,000 for air at 298 K in the geometry shown).

The wall shear was determined by:

$$\tau_W = \mu \frac{\partial u}{\partial n}$$

where μ is the dynamic viscosity of the fluid and the partial differential is the velocity gradient in the fluid adjacent to the no-slip defined wall, i.e. the sample surface in Figure 3. The grid resolution at the surface was important for resolving this gradient and a face sizing scheme was imposed here to ensure sufficient detail capture.

The wall pressure was determined from the local flow field details.

3 Results

3.1 Sample summary

The samples that were produced as outlined above conformed to the general volume percentage ratios of 35 vol% C_f (0/90° orientation), 65 vol% matrix (85% ZrB_2 + 10% SiC + 5% Y_2O_3). The masses and densities of the produced samples are shown in Table 1.

The microstructure of the as-produced material is shown in Figure 4.

Fibres were homogeneously distributed across the composite, with most fibres individually surrounded by a layer of ceramic matrix (Figure 4b). SiC was found as small particles at ZrB_2 grain boundaries and occasionally as agglomerates. The latter likely originated from a non-homogeneous dispersion in the powder suspension used for slurry infiltration. The fibre/matrix interface was strong, as evidenced by the high magnification micrograph (Figure 4c) where the outer fibre surface has partially reacted with the matrix, and from the fracture surface (Figure 4d) showing the short extent of fibre pull-out (< 20 µm). The porosity, obtained as the difference from the relative density value, amounted to less than 5 vol%.

3.2 Ablation analysis

The characteristic ablation patterns for each angle of attack investigated are shown in Figure 5. The shape, size and aspect ratio of the oxidised areas changed as the angle of attack was reduced from 90° to 10°. As expected, this change was from a circular, radially symmetric oxidation morphology to a skewed ellipse.

The width, length and area of the damaged samples as determined by image analysis are shown in the Figure 6a. The oxidised width, the dimension indicated in Figure 5c, can be seen to increase by a greater margin than the damage length as the angle changes.

Figure 7 shows the temperature distribution as determined by IR thermography across the indicated surface line segment. At higher angles of attack, the temperature distribution across the indicated bisecting line show that both the peak temperature increased and the temperature distribution became more symmetrical. This is matched by the obvious decrease in aspect ratio to circular at 90° compared to those at 30° and 10°.

$\Delta m/\Delta t$ is displayed in Figure 8, with 3 different samples being tested at each angle. $\Delta m/\Delta t$ can be seen to increase slightly as the angle of attack was decreased, i.e. grazing angles were less damaging in terms of material removal than a direct, 90° angle of attack. It should be noted, however, that one of the samples tested at 90° showed significant variability in its results compared to the other two, far more than for any of the other angles. The probable reason for this was an error in distance, set at the beginning of the test. Since there was no opportunity to retest a fresh sample, this data point has been excluded from the analysis.

The peak static pressure and wall shear from the modelling results are shown in Figure 9a. As the angle of attack increased from 10° to 90° the wall shear increased markedly, by 1.5x, whilst the surface static pressure was reduced by a far higher proportion, almost 0.1x the value at 90°. Comparing this value to the integrated value over the work surface in Figure 9b, they can be seen to follow the same trend (though note the change in units). It is important to consider the changing surface area of the analysis surface, which can be expected to vary as shown in Figure 10. Given the concentration of large magnitudes of both static pressure and wall shear around the torch tip in all cases, however, the 'extra area' the integral is calculated over does not result in a significant increase in either variable.

XRD analysis, Table 2, showed that phases other than $t\text{-}ZrO_2$ were largely absent from the surface in the oxidised areas of the test specimens, excluding that for the 10° sample, for which there is evidence of the unreacted starting materials.

SEM imaging of the post-test samples are shown in Figure 11. For the samples tested at 90°, a large grained microstructure resulted in the centre of the damage area, Figure 10 (a), possibly from melt-solidification. Large, ~2 μm, round pores were found in the surface, perhaps indicative of outgassing of volatile by-products, e.g. $SiO_{(g)}$ and $B_2O_{3(g)}$. Further away from this central region, Figure 10 (b), the surface shows sub-micron texturing suggesting nanograined $t\text{-}ZrO_2$, bound together with large pores. The central region of the 30° sample, Figure 10 (c), shows similar pore sizes as the 90° sample, but with significantly smaller zirconia grains and with significantly greater roughness. In the outer oxidised region, Figure 10 (d), fine ZrO_2 grains can be seen dispersed in a silicate glass. These morphologies are repeated in the 10° sample, Figures 10 (e) and (f), with fewer pores and larger structure sizes than in the 30° case. SEM analysis detected traces of Si in both the central and more distant regions. Figure 12 shows that nano ZrO_2 grains were embedded in a glassy matrix. This corroborates the results from Raman spectroscopy; formation of a biphasic $ZrO_2\text{-}SiO_2$ network was preferred over formation of a zirconium silicate glass.

4 Discussion

From the image analysis, the "peak damage point" was identified as the highest contrast part of the surface, indicating the highest level of oxidation, along the vector indicated in Figure 5b. The distance from the up-wind onset of the oxidation damage (i.e. the surface distance between this central point and the damaged part of the surface closest to the torch tip) was

measured during image analysis and compared against the peak temperature along the line indicated in Figure 5b. Figure 13 shows the total oxidised width along that vector – the distance into the oxidised area the peak temperature and peak damage location coincide with – and the % across the whole oxidised area at which the peak damage location exists. This shows that the peak damage position tracks the peak temperature closely across the range of angle of attack and that this location migrates into the centre from the up-wind direction of the damage area as the angle of attack increases to 90°. This is what would be expected for the case of the gas flow being normal to the surface – a circular damage area.

$\Delta m/\Delta t$ shows a slight positive increase as the angle of attack is reduced and can be combined with the oxidised area to produce a specific $\Delta m/\Delta t$; a mass change per unit area of oxidised surface. This is shown in Figure 14, combined with the peak temperature (Figure 14a), integrated pressure from the modelling (Figure 14b) and integrated wall shear (Figure 14c). The specific $\Delta m/\Delta t$ can be seen to correlate with the change in integrated wall shear over the sample surface. It also correlates inversely with both temperature and pressure. As the $\Delta m/\Delta t$ value is a balance between the mass gain due to the formation of the denser oxide products (when comparing to SiC and ZrB_2) and the mass loss due to their displacement from the surface, a positive value indicates either that more oxide is being produced, or that less material is being displaced. Figure 6a shows that less oxide is being produced as the angle of attack is reduced. This is likely explained by the thermographic line scans indicated in Figure 7 – much of the sample surface is of a lower temperature when the angle of attack is oblique. Hence, the larger value of $\Delta m/\Delta t$ for the oblique angles of attack must be a result of reduced material removal compared to the 90° case. This is prominent, given the reduced production of oxide.

The temperature changes can adequately explain many of the microstructural differences observed in the SEM analysis. The highest temperature regime, 90°, showed that a melt had existed that consisted of ZrO_2. Allowing for both the quoted error range of the pyrometer (0.5%, which is equivalent to ±15°C) and other factors such as the non-constant emissivity ratio between the two pyrometer channels over the course of the heating, the measured peak surface temperature of 2640°C is close to the approximate melting point of YSZ of 2680°C [24]. The flat surface morphology, large grain sizes and large round bubbles corroborate this observation. The shallower angles of attack, 30° and 10°, do not share this morphology, corresponding with the lower measured peak temperatures over the course of the ablation; 2370°C and 2230°C, respectively. The surfaces of these samples are similar: pores exist where gas may have escaped from the central region, possibly due to the active oxidation of SiC or evaporation of B_2O_3/SiO_2. This behaviour is consistent with the decreased temperature, as is the existence of the glassy phases on the periphery of the sample surfaces. At these similar distances from the 'hot zone' in the 90°C sample, Si is still not detected by EDS and a fine-grained, single phase ZrO_2 region is seen.

On this basis, it is likely that the damage behaviour seen over the angle range is line with the peak temperature and distribution. The lower temperatures may be caused by the presumed lower residence time of the hot gases at the surface. The distance travelled by the flame gas is reduced for the oblique cases compared to the 90° case. In the latter, the flame must bend through a right angle at the surface, requiring significant redirection of the gas stream and loss of momentum. In the oblique case, it does not – only a slight adjustment is required and much of the gas stream velocity can be retained. However, being directed in one direction (the plane in which the surface is tilted relative to the flame), the hot gas spreads out less in other directions and meets a lower amount of 'oxidisable' surface. The increased velocity is evidenced by the increased shear force at the surface of the sample shown in Figure 9b at lower angles of attack. There was no indication that this increased force increased the damage on the sample surface. It is unlikely that the correlation shown in Figure 14c, specific $\Delta m/\Delta t$

with shear force, is more than coincidental – it seems more plausible from a physical point of view for the reduced damage to result from reduced temperature, rather than increased shear force. The failure of this study to separate the temperature variable properly from the pressure and shear force variables means that an authoritative comment on the effects of shear force and stagnation pressure on surface oxide species (friable solids or melts) is not possible. It might have been possible to separate these variables using samples with higher thermal resistance. Alternatively, using gas jets in combination with laser heating may have yielded an orthogonal variable testing environment that allowed the independent analysis of the shear and static pressure effects, subsequently potentially permitting greater insight.

The fact that the 90° sample lost most mass but was most oxidised, indicates the importance of the static pressure; the 10° or 30° samples had comparatively low static pressures. While the three variables – temperature, static pressure and shear force – were not fully separated in this study, the results for 90° do indicate that the highest-pressure sample experienced most mass loss. However, these were also the only samples which produced a molten phase during testing – it is possible this phase change resulted in a far more easily displaced/vaporisable component. The mass loss may have resulted from easily volatilised ZrO_2 or SiO. The reducing trend in $\Delta m/\Delta t$ as the angle of attack was increased was mirrored by the increase in pressure. This highlights that, for a material that did not produce a melt at most angles, the vastly heightened static pressure was more likely responsible for material removal than the shear forces. In essence, more oxide was formed at high angles of attack and correspondingly there was greater pressure-assisted denudation.

5 Conclusion

The same torch heat flux and gas flow rate were used to provide a number of ablation environments for a UHTCMC material by the variation of the ablation angle of attack from 90° (perpendicular to the surface) down to 10°.

Experimentally, it was found that smaller angles of attack induced lower surface temperatures, and a higher $\Delta m/\Delta t$ per unit of damaged surface. This correlated microstructurally with the formation of a rough, asperity-dense surface that did not develop a melt during testing. These samples showed a lower extent of oxidation morphologically and a higher mass gain relative to the 90° samples. This suggested that the increased amount of oxide, volumetrically denser, was offset by increasing material loss at more direct (i.e. closer to 90°) angles of attack.

To corroborate this, rudimentary fluid dynamics calculations were performed which indicated higher static pressure across the sample surface in the cases of direct angles of attack, which, in turn, corresponded with the reduced specific $\Delta m/\Delta t$. This analysis was rudimentary in the sense that the temperatures, viscosities and surface dynamics were not taken into account and the simulation was steady-state (not time resolved), hence the specific values produced were only relative measures.

The value of this work is that it has revealed another mode for which material response may be probed via OAT testing; a particularly high-shear, low temperature and pressure regime. The latter environment may be expected downwind of stagnation points in many components relevant in the aerodynamic environment. Angled testing can mirror certain aspects of this and demonstrate not only the different material responses but also provide information on the protection mechanisms that are relevant under the different conditions. This further enhances the cost-effectiveness of OAT set-ups as rapid material screening tools.

References

[1]   D.M. Van Wie, D.G. Drewry, D.E. King, C.M. Hudson, The hypersonic environment: Required operating conditions and design challenges, J. Mater. Sci. 39 (2004) 5915–5924. https://doi.org/10.1023/B:JMSC.0000041688.68135.8b.

[2]   L. V Kravchuk, K.P. Buiskikh, I.A. Gusarova, A.M. Potapov, N.N. Feofentov, Methods for the Simulation of the Aerodynamic Heating Conditions of the Structural Elements of Space Shuttles, Strength Mater. 50 (2018) 565–574. https://doi.org/10.1007/s11223-018-0002-x.

[3]   E.P. Simonenko, D. V Sevast'yanov, N.P. Simonenko, V.G. Sevast'yanov, N.T. Kuznetsov, Promising ultra-high-temperature ceramic materials for aerospace applications, Russ. J. Inorg. Chem. 58 (2013) 1669–1693. https://doi.org/10.1134/S0036023613140039.

[4]   S. Tang, C. Hu, Design, Preparation and Properties of Carbon Fiber Reinforced Ultra-High Temperature Ceramic Composites for Aerospace Applications: A Review, J. Mater. Sci. Technol. 33 (2017) 117–130. https://doi.org/https://doi.org/10.1016/j.jmst.2016.08.004.

[5]   W.G. Fahrenholtz, G.E. Hilmas, Ultra-high temperature ceramics: Materials for extreme environments, Scr. Mater. 129 (2017) 94–99. https://doi.org/https://doi.org/10.1016/j.scriptamat.2016.10.018.

[6]   L. Li, Y. Wang, L. Cheng, L. Zhang, Preparation and properties of 2D C/SiC–ZrB2–TaC composites, Ceram. Int. 37 (2011) 891–896. https://doi.org/https://doi.org/10.1016/j.ceramint.2010.10.033.

[7]   P. Sarin, P.E. Driemeyer, R.P. Haggerty, D.K. Kim, J.L. Bell, Z.D. Apostolov, W.M. Kriven, In situ studies of oxidation of ZrB_2 and ZrB_2–SiC composites at high temperatures, J. Eur. Ceram. Soc. 30 (2010) 2375–2386. https://doi.org/https://doi.org/10.1016/j.jeurceramsoc.2010.03.009.

[8]   A.K. Kuriakose, J.L. Margrave, The Oxidation Kinetics of Zirconium Diboride and Zirconium Carbide at High Temperatures, J. Electrochem. Soc. 111 (1964) 827–831. https://doi.org/10.1149/1.2426263.

[9]   X. Feng, X. Wang, Y. Liu, W. Tian, M. Zhang, X. Jian, L. Yin, L. Zhang, J. Xie, L. Deng, Pursuing enhanced oxidation resistance of ZrB2 ceramics by SiC and WC co-doping, J. Eur. Ceram. Soc. 38 (2018) 5311–5318. https://doi.org/https://doi.org/10.1016/j.jeurceramsoc.2018.07.041.

[10]   K. Gürcan, E. Ayas, In-situ synthesis and densification of HfB_2 ceramics by the spark plasma sintering technique, Ceram. Int. 43 (2017) 3547–3555. https://doi.org/https://doi.org/10.1016/j.ceramint.2016.11.164.

[11]   L. Silvestroni, S. Failla, I. Neshpor, O. Grigoriev, Method to improve the oxidation resistance of ZrB_2-based ceramics for reusable space systems, J. Eur. Ceram. Soc. 38 (2018) 2467–2476. https://doi.org/https://doi.org/10.1016/j.jeurceramsoc.2018.01.025.

[12]   J. Binner, M. Porter, B. Baker, J. Zou, V. Venkatachalam, V.R. Diaz, A. D'Angio, P. Ramanujam, T. Zhang, T.S.R.C. Murthy, Selection, processing, properties and applications of ultra-high temperature ceramic matrix composites, UHTCMCs – a review, Int. Mater. Rev. (2019) 1–56. https://doi.org/10.1080/09506608.2019.1652006.

[13]   E. Eakins, D.D. Jayaseelan, W.E. Lee, Toward Oxidation-Resistant ZrB_2-SiC Ultra High Temperature Ceramics, Metall. Mater. Trans. A. 42 (2011) 878–887.

https://doi.org/10.1007/s11661-010-0540-8.

[14] X. Yao, H. Li, Y. Zhang, H. Wu, X. Qiang, A SiC–Si–ZrB$_2$ multiphase oxidation protective ceramic coating for SiC-coated carbon/carbon composites, Ceram. Int. 38 (2012) 2095–2100. https://doi.org/https://doi.org/10.1016/j.ceramint.2011.10.047.

[15] R. Savino, M. De Stefano Fumo, D. Paterna, A. Di Maso, F. Monteverde, Arc-jet testing of ultra-high-temperature-ceramics, Aerosp. Sci. Technol. 14 (2010) 178–187. https://doi.org/https://doi.org/10.1016/j.ast.2009.12.004.

[16] C. Carney, D. King, M. De Stefano Fumo, C. Purpura, E. Trifoni, A. Martucci, B. Larson, T. Parthasarathy, M. Cinibulk, G. Marino, Oxidation response of a SiCf/SiC CMC with a HfB$_2$-based coating in an arc jet test, Adv. Appl. Ceram. 117 (2018) s19–s25. https://doi.org/10.1080/17436753.2018.1509174.

[17] V. V Kurbatkina, E.I. Patsera, E.A. Levashov, A.N. Timofeev, Self-propagating high-temperature synthesis of refractory boride ceramics (Zr,Ta)B$_2$ with superior properties, J. Eur. Ceram. Soc. 38 (2018) 1118–1127. https://doi.org/https://doi.org/10.1016/j.jeurceramsoc.2017.12.031.

[18] A. Paul, S. Venugopal, J.G.P. Binner, B. Vaidhyanathan, A.C.J. Heaton, P.M. Brown, UHTC–carbon fibre composites: Preparation, oxyacetylene torch testing and characterisation, J. Eur. Ceram. Soc. 33 (2013) 423–432. https://doi.org/https://doi.org/10.1016/j.jeurceramsoc.2012.08.018.

[19] Y. Liu, Q. Fu, J. Zhang, L. Li, L. Zhuang, Erosion resistance of C/C-SiC-ZrB$_2$ composites exposed to oxyacetylene torch, J. Eur. Ceram. Soc. 36 (2016) 3815–3821. https://doi.org/https://doi.org/10.1016/j.jeurceramsoc.2016.04.007.

[20] C. Yan, R. Liu, B. Zha, C. Zhang, Fabrication and properties of 3-dimensional 4-directional Cf/HfC-SiC composites by precursor impregnation and pyrolysis process, J. Alloys Compd. 739 (2018) 955–960. https://doi.org/https://doi.org/10.1016/j.jallcom.2017.12.059.

[21] A. Paul, J.G.P. Binner, B. Vaidhyanathan, A.C.J. Heaton, P.M. Brown, Heat flux mapping of oxyacetylene flames and their use to characterise Cf-HfB$_2$ composites, Adv. Appl. Ceram. 115 (2016) 158–165. https://doi.org/10.1080/17436753.2015.1104050.

[22] J. Marschall, D.G. Fletcher, High-enthalpy test environments, flow modeling and in situ diagnostics for characterizing ultra-high temperature ceramics, J. Eur. Ceram. Soc. 30 (2010) 2323–2336. https://doi.org/https://doi.org/10.1016/j.jeurceramsoc.2010.01.010.

[23] J. Crafton, C. Carter, G. Elliott, J. Sullivan, The impingement of sonic and sub-sonic jets onto a flat plate at inclined angles, Exp. Fluids. 41 (2006) 699. https://doi.org/10.1007/s00348-006-0192-z.

[24] P. Barreiro, P. Rey, A. Souto, F. Guitián, Porous stabilized zirconia coatings on zircon using volatility diagrams, J. Eur. Ceram. Soc. 29 (2009) 653–659. https://doi.org/https://doi.org/10.1016/j.jeurceramsoc.2008.07.018.

List of figures

Figure 1: Plan image of variable angle torch test rig. The angle and sample x-y co-ordinate centre may be varied using the array of drilled holes to ensure precise angle and test distances.
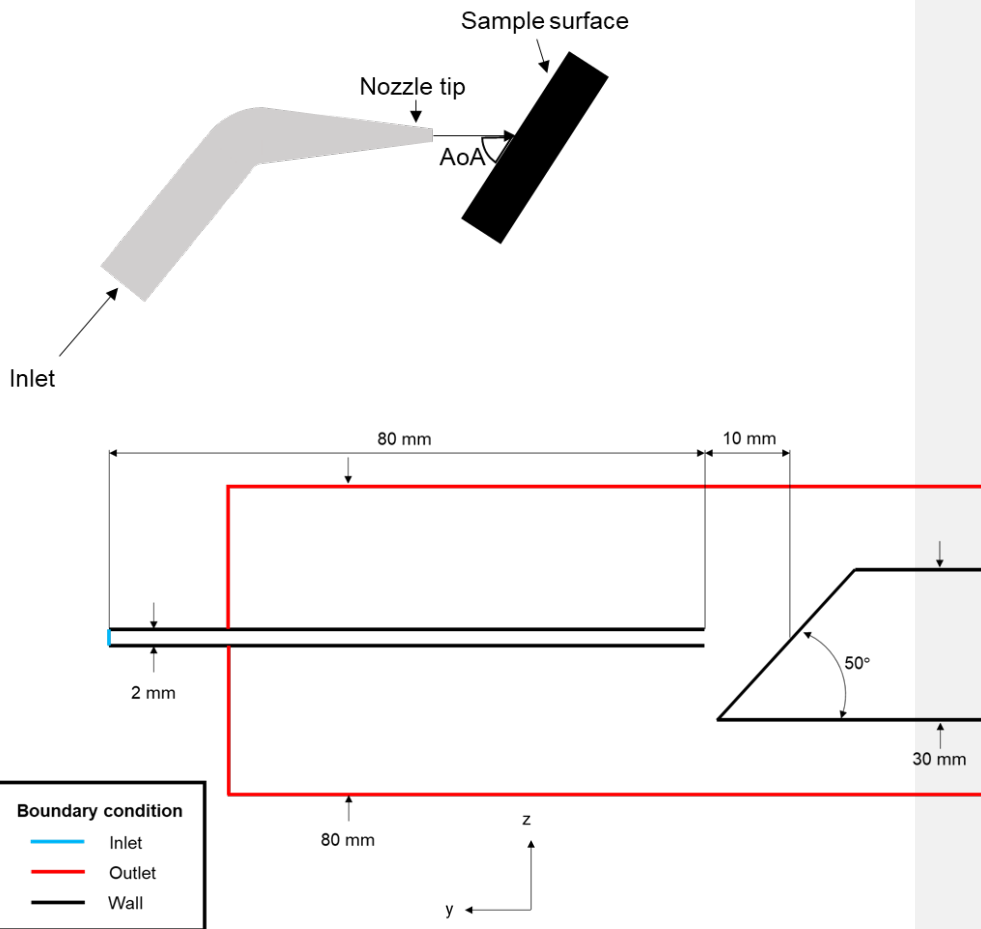
Figure 2: A schematic in 2D of the geometry used in the flow modelling calculations, with a schematic of the features of the test being represented. Red indicates pressure outlet conditions, black indicates interior wall boundary conditions and blue indicates the velocity inlet.
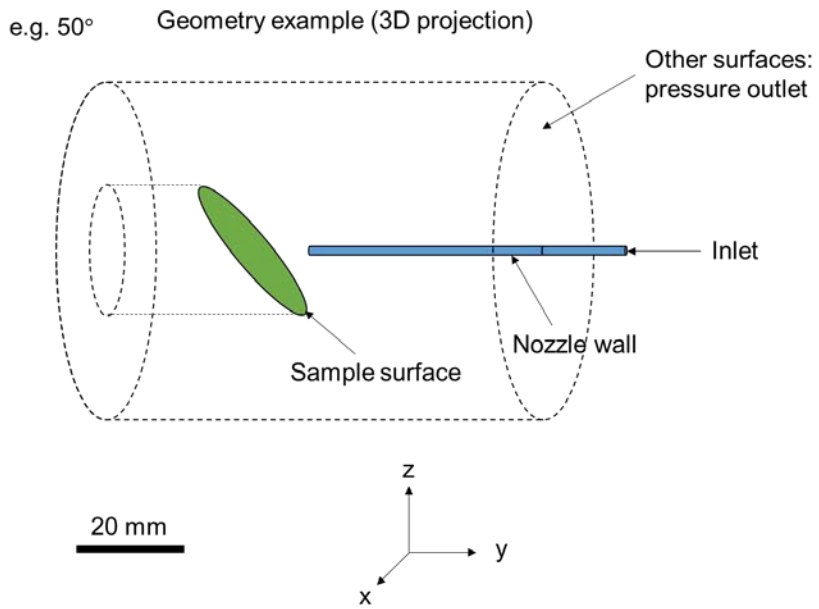
e.g. 50°   Geometry example (3D projection)

Other surfaces:
pressure outlet

Inlet

Nozzle wall

Sample surface

z

y

x

20 mm

Figure 3: A 3D representation of the geometry used in the fluid dynamics calculations.
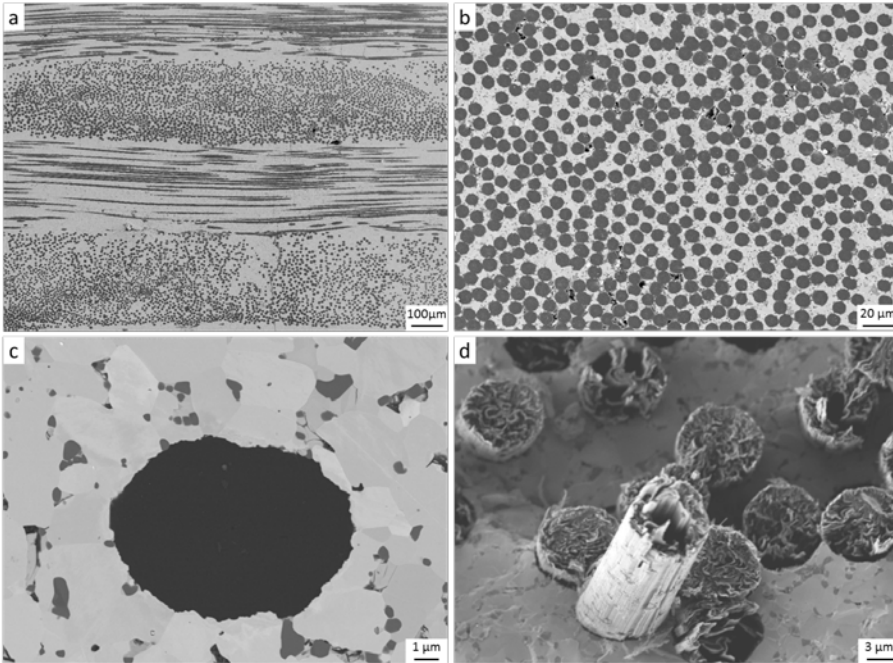
Figure 4: Microstructure of the pristine sample: a) 0/90° layer configuration where the UHTC matrix is in white and the fibres in black, b) homogeneous fibre distribution in the matrix, c) fibre/matrix interface, d) fibre pull-out
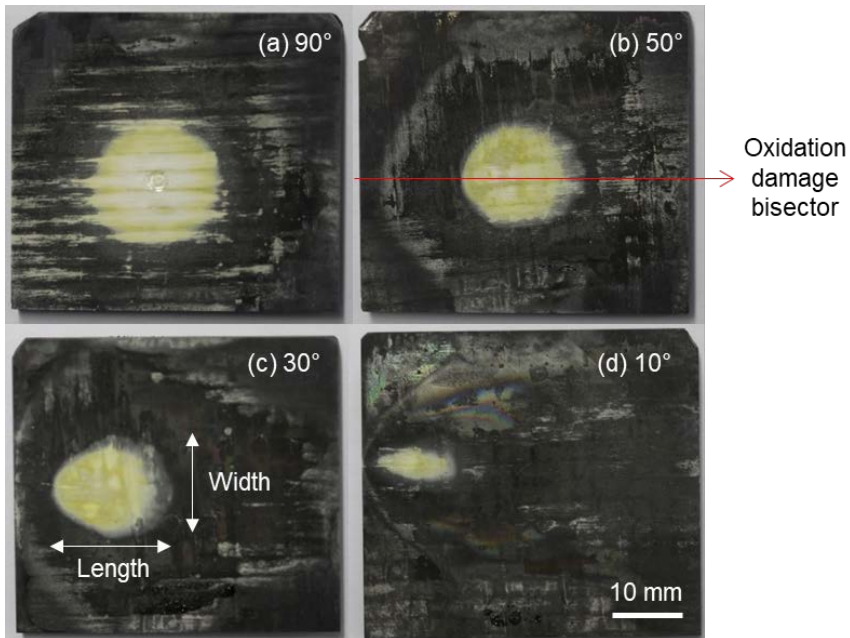
Figure 5: The characteristic ablation morphologies post-test by angle; (a) 90°, (b) 50°, (c) 30° and (d) 10°. The total thresholded damage area and individual lengths, horizontally and vertically, of the ablation morphologies resulting from the angled torch testing are shown in Figure 6. The vector used in the determination of the 'peak damage point' distance in Figure 13 is shown schematically in 5(b).

Damage area

Damage dimensions
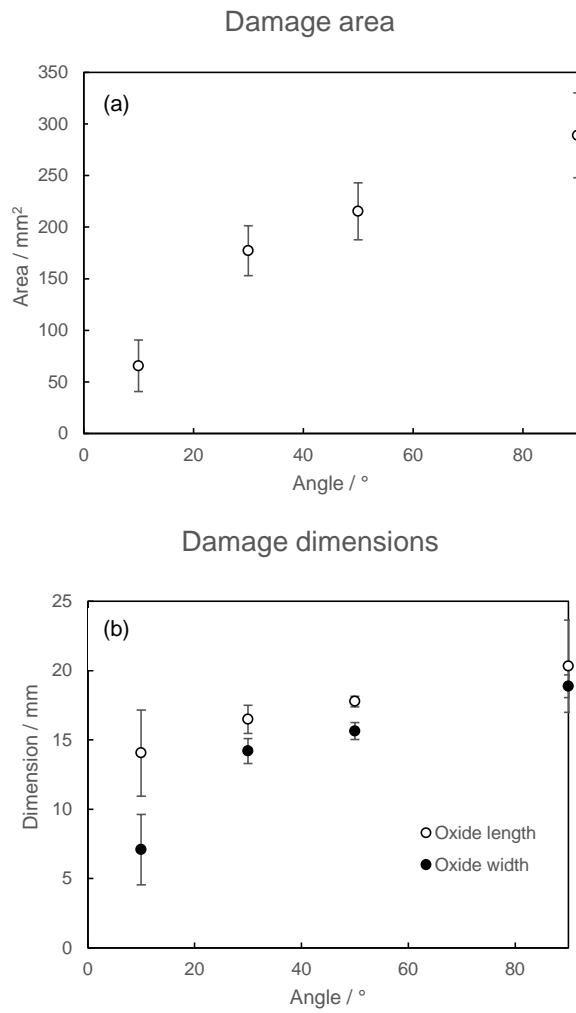
Figure 6: The total thresholded damage area and individual length as defined in Figure 5c of the ablation morphologies resulting from the angled torch testing.
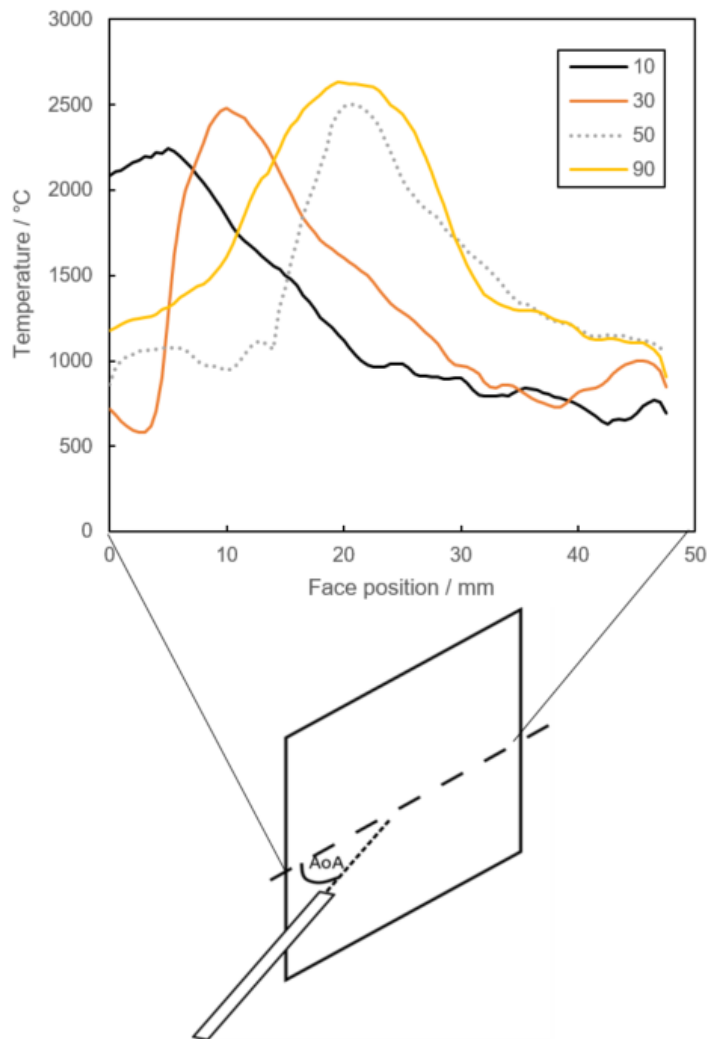
Figure 7: The thermographic line scans of four samples taken at each incident angle condition. The line scan was collected over the bisector indicated in Figure 5b in all cases.
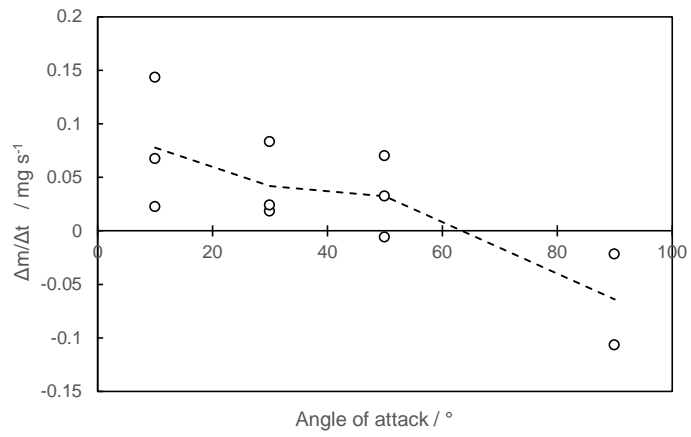
Figure 8: Δm/Δt distribution as a function of incident angle. Three different samples were tested at each angle. The dashed line is guide for the eye
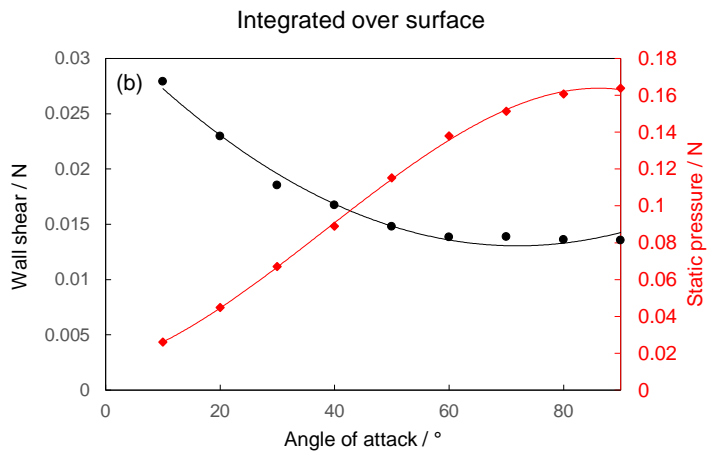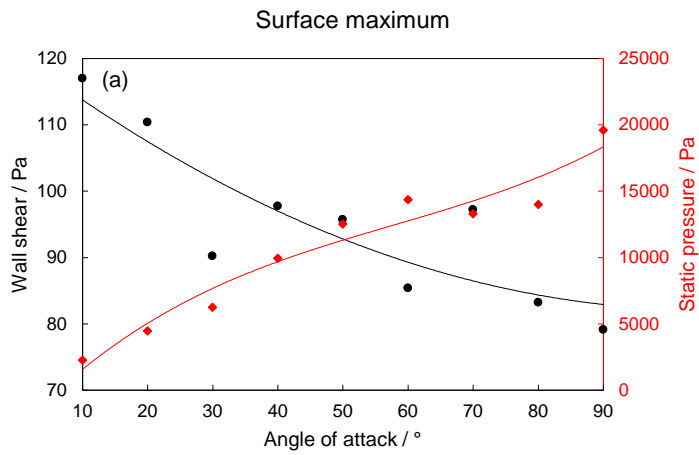
Figure 9: The output from the fluid dynamics calculations. (a) The wall shear and pressure maxima on the sample surface; (b) the integrated wall shear and pressures over the sample surface.
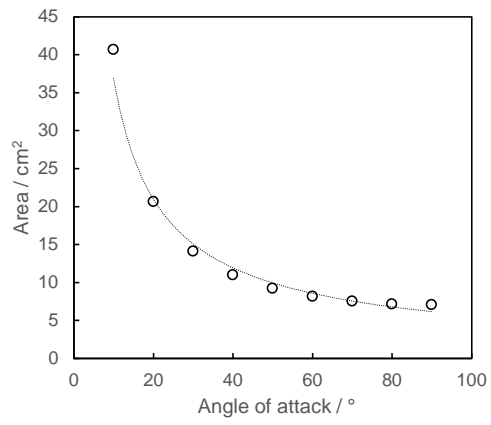
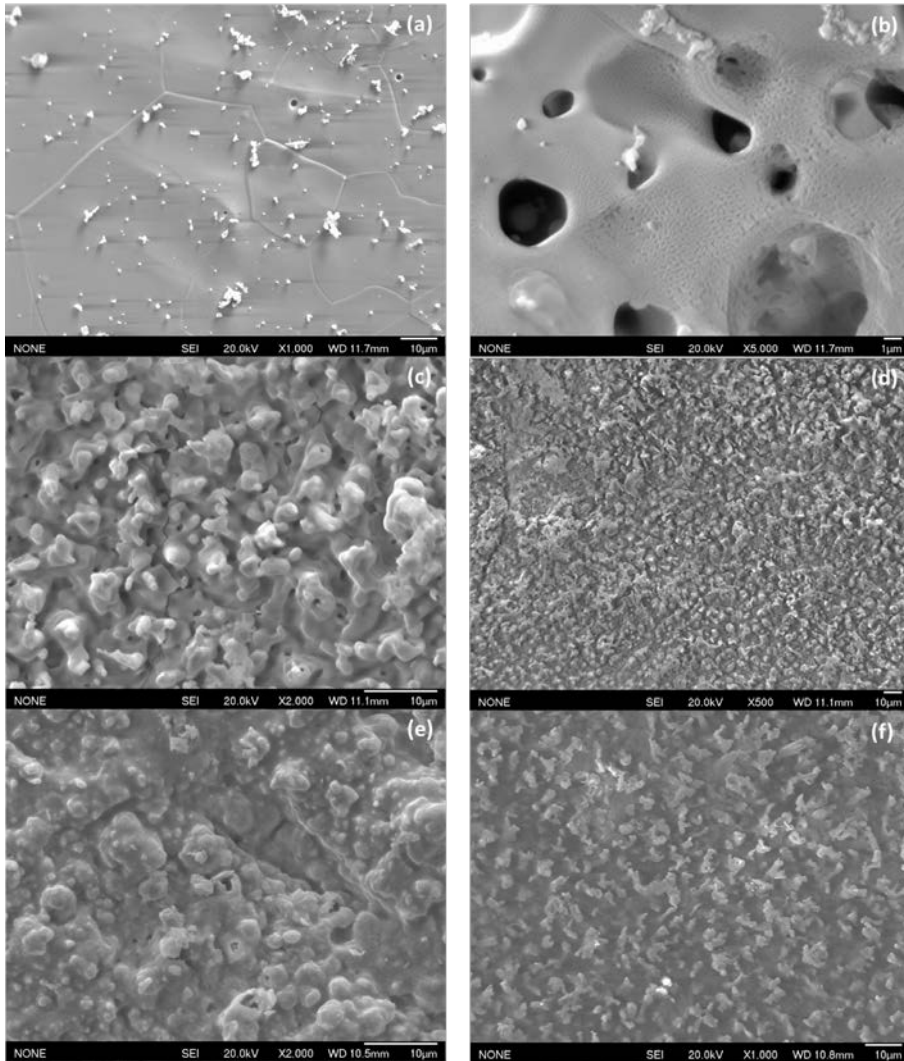Figure 10: The angular dependence of the sample surface area.

Figure 11: SEM images of the post-ablation surface morphologies. (a, c & e) were collected at the centres of the ablated regions; (b, d & f) were collected at the extremities of the oxidised region. (a & b) were tested at 90°, (c & d) at 30° and (e & f) at 10°.
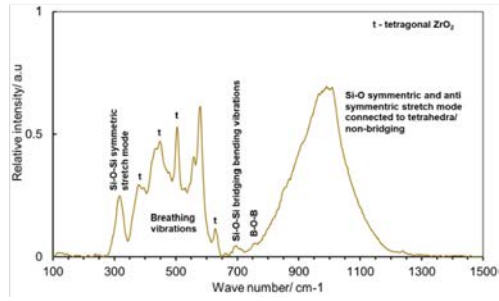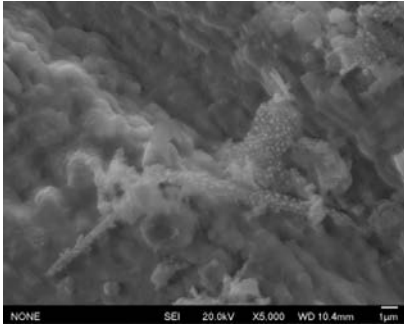
Figure 12: A high magnification SEM image of the 30° test condition showing nano-ZrO$_2$ grains embedded in a glassy matrix. The distinct peaks for these phases are shown in the accompanying Raman spectrogram.
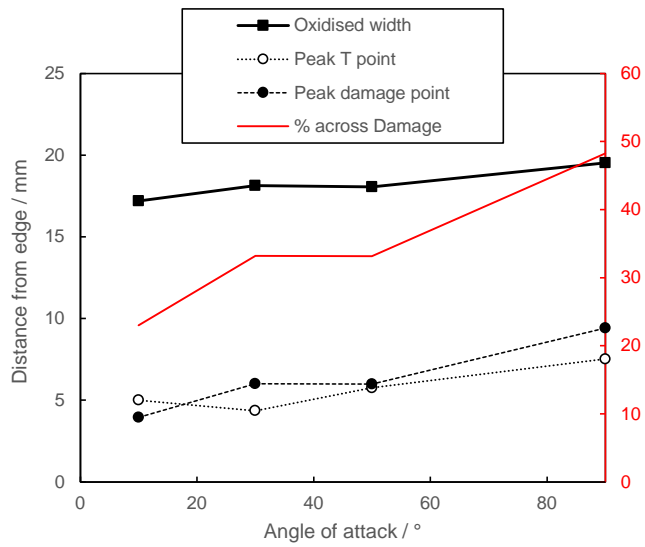
Figure 13: The central ablation point (highest contrast ablated region) for four samples, compared to the peak temperature location along the surface vector indicated in Figure 6.
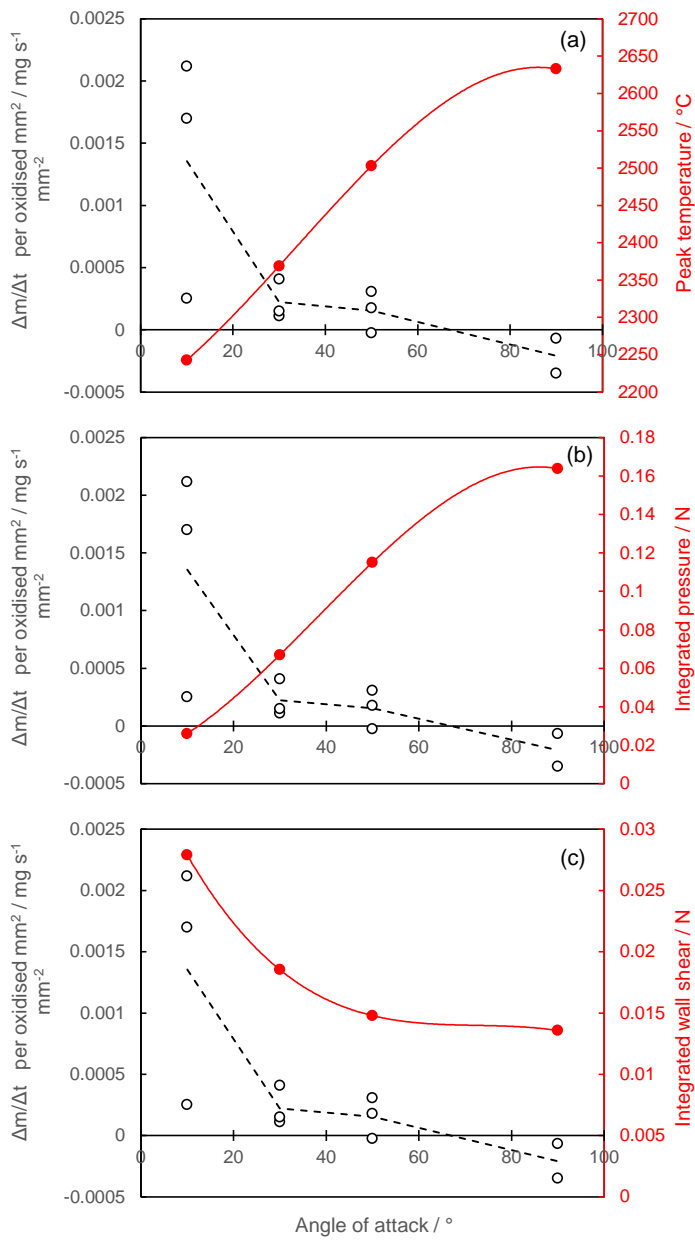
Figure 14: The correlation of the specific Δm/Δt with the (a) peak temperature measured and the fluid dynamics calculation outputs, (b) integrated pressure and (c) integrated wall shear.

Table 1: The specification of the as-produced samples.

Sample #	Mass / g	Dimensions / mm			Density / g cm^{-3}	
		Width	Length	Height	Archimedes	Geometric
C3_CNR_197	61.7862	43.59	48.09	7.09	4.20	4.16
C3_CNR_198	62.369	43.55	48	7.14	4.10	4.18
C3_CNR_199	62.2162	43.47	47.9	7.05	4.10	4.24
C3_CNR_200	62.8532	43.5	48.01	7.16	4.17	4.20
C3_CNR_201	61.5811	46.56	48.09	7.11	4.15	3.87
C3_CNR_202	63.0687	43.53	47.04	7.14	4.32	4.31
C3_CNR_203	62.4286	43.55	47.76	7.16	4.20	4.19
C3_CNR_204	62.6423	43.54	47.92	7.18	4.20	4.18
C3_CNR_205	65.3159	43.72	47.98	7.47	4.11	4.17
C3_CNR_206	67.2917	43.51	48.02	8.18	3.99	3.94
C3_CNR_207	64.2994	43.45	48.07	8.12	3.82	3.79
C3_CNR_208	71.1053	43.55	47.73	8.15	4.24	4.20

Table 2: The phases identified from XRD analysis of the oxide sales of the post-ablation sample surfaces

Angle of attack / °	Predominant phases present in sample centre
10	ZrB_2, SiC, t-ZrO_2, Y_2O_3
30	t-ZrO_2
50	t-ZrO_2
90	t-ZrO_2